



LAWRENCE  
LIVERMORE  
NATIONAL  
LABORATORY

# Propagation of Shear Alfvén waves in two-ion species plasmas confined by a nonuniform magnetic field

W. A. Farmer, G. J. Morales

June 11, 2013

Physics of Plasmas

## **Disclaimer**

---

This document was prepared as an account of work sponsored by an agency of the United States government. Neither the United States government nor Lawrence Livermore National Security, LLC, nor any of their employees makes any warranty, expressed or implied, or assumes any legal liability or responsibility for the accuracy, completeness, or usefulness of any information, apparatus, product, or process disclosed, or represents that its use would not infringe privately owned rights. Reference herein to any specific commercial product, process, or service by trade name, trademark, manufacturer, or otherwise does not necessarily constitute or imply its endorsement, recommendation, or favoring by the United States government or Lawrence Livermore National Security, LLC. The views and opinions of authors expressed herein do not necessarily state or reflect those of the United States government or Lawrence Livermore National Security, LLC, and shall not be used for advertising or product endorsement purposes.

# Propagation of Shear Alfvén waves in two-ion species plasmas confined by a nonuniform magnetic field

W. A. Farmer<sup>1,2</sup> and G. J. Morales<sup>1</sup>

<sup>1</sup>Physics and Astronomy Department,  
University of California, Los Angeles  
Los Angeles, California 90095

<sup>2</sup>Lawrence Livermore National Laboratory  
Livermore, CA 94550, USA

## Abstract

Ray tracing calculations are performed for shear Alfvén waves in two-ion species plasmas in which the magnetic field varies with position. Three different magnetic topologies of contemporary interest are explored: a linear magnetic mirror, a pure toroidal field, and a tokamak field. The wave frequency is chosen to lie in the upper propagation band, so that reflection at the ion-ion hybrid frequency can occur for waves originally propagating along the magnetic field direction. Calculations are performed for a magnetic well configuration used in recent experiments [S. T. Vincena, *et al.*, Geophys. Res. Lett. **38**, L11101, (2011); S. T. Vincena, *et al.*, Phys. Plasmas, **20**, 012111 (2013)] in the Large Plasma Device (LAPD) related to the ion-ion hybrid resonator. It is found that radial spreading cannot explain the relatively low values of the resonator quality factor ( $Q$ ) measured in those experiments, even when finite ion temperature is considered. This identifies that a damping mechanism is present that is at least an order of magnitude larger than dissipation due to radial energy loss. Calculations are also performed for a magnetic field with pure toroidal geometry, without a poloidal field, as in experiments being planned for the Enormous Toroidal Plasma Device (ETPD). In this case, the effects of field-line curvature cause radial reflections. A poloidal field is included to explore a tokamak geometry with plasma parameters expected in ITER. When ion temperature is ignored, it is found that the ion-ion hybrid resonator can exist and trap waves for multiple bounces. The effects of finite ion temperature combine with field line curvature to cause the reflection point to move towards the tritium cyclotron frequency when electron temperature is negligible. However, for ITER parameters, it is shown that the electrons must be treated in the adiabatic limit to properly describe resonator phenomena.

**PACS:** 52.35 Bj, 52.50 Qt, 52.55Pi

LLNL - JRNL - 638705

## I. INTRODUCTION

In a magnetized plasma with two ion species, the perpendicular component of the cold-plasma dielectric coefficient,  $\epsilon_{\perp}$ , can vanish at a frequency known as the ion-ion hybrid frequency [1,2],

$$\omega_{ii} = \frac{\omega_{p1}^2 \Omega_2^2 + \omega_{p2}^2 \Omega_1^2}{\omega_{p1}^2 + \omega_{p2}^2}, \quad (1)$$

where  $\omega_{pj}$  and  $\Omega_j$  refer respectively to the ion plasma frequency and the ion cyclotron frequency of species  $j$ . The vanishing of  $\omega_{ii}$  causes a collective resonance for waves propagating across the confinement magnetic field, typically the compressional or fast Alfvén wave. This resonance has been exploited in schemes used to heat minority ion species in magnetically confined plasmas [3-7]. In contrast, for the shear (or the slow) Alfvén wave that propagates primarily along the confinement magnetic field, the ion-ion hybrid acts as a cutoff and not a resonance. This property can be seen by examining the dispersion relation for shear waves with large perpendicular wave number,  $k_{\perp}$ ,

$$k_{\parallel} = k_0 \sqrt{\epsilon_{\perp} \left[ 1 - k_{\perp}^2 / k_0^2 \epsilon_{\parallel} \right]}, \quad (2)$$

where  $k_{\parallel}$  is the parallel wave number for frequency  $\omega$ ,  $k_0 = \omega/c$  with  $c$ , the speed of light, and  $\epsilon_{\parallel}$ , the dielectric coefficient parallel to the confinement magnetic field. Here, large perpendicular scale means that  $k_{\perp} c / \omega_{pi} \gg 1$ , or that the perpendicular wavelength is much less than the smallest ion skin-depth. When this condition is violated, coupling between the compressional and shear Alfvén waves occurs, and the expression given by Eq. (2) is not adequate. Under such conditions, the off-diagonal component of the dielectric tensor,  $\epsilon_{xy}$ , must be included in the formulation of the dispersion relation leading to a more complicated expression.

The wave cut-off at the ion-ion hybrid frequency leads to a propagation gap in which the shear wave is evanescent, occurring over the frequency range,  $\Omega_1 \leq \omega \leq \omega_{ii}$ , where  $\Omega_1$  is the gyrofrequency of the heavier ion species. This separates the propagating frequency range for shear waves into two bands,  $\omega < \Omega_1$  and  $\omega_{ii} < \omega < \Omega_2$ . When a shear wave in the upper frequency band propagates into a region of increasing magnetic field, the wave reflects at the position where the frequency of the wave matches the local value of the ion-ion hybrid frequency. This feature has been confirmed by experiments in linear devices [8] and tokamaks [9]. It is possible for a magnetic well to form a natural resonator for the shear waves, since two conjugate reflection points trap the wave, confining the energy. It has been proposed that this type of resonator should naturally exist in planetary



magnetospheres. Guglielmi *et al.* [10] calculated the resonator spectrum and compared it to satellite observations, but they were unable to confirm the existence of the resonator. Moiseenko and Tennfors [11], motivated by analogies to low frequency toroidicity-induced Alfvén eigenmodes (TAE), have considered the role of vanishing  $\varepsilon_{\perp}$  in tokamak geometry. The authors identified a new class of high-frequency toroidal eigenmodes that they named TLE (or TAE-like eigenmodes), but they did not explore the possibility of a resonator. A recent study by the present authors [12] has raised the possibility of a resonator existing in a burning plasma, but the study used a one-dimensional model and neglected the complicating geometrical effects that exist in a tokamak. The resonator has been verified experimentally [13] in the Large Plasma Device (LAPD) at the University of California, Los Angeles (UCLA). In that study, shear waves were launched in a linear device with a magnetic well configuration. Resonances were observed when the antenna was operated in both single frequency scans and pulsed configurations. The quality factors (Q) of the resonances were observed to be between 11 and 18, a value much smaller than expected from cold plasma theory considerations [14].

For a specific magnetic well geometry, ray tracing studies are useful in determining the degree to which the wave energy can be trapped. Rauch and Roux performed ray tracing studies in a dipole magnetic geometry for a cold plasma [15] in an effort to explain GEOS 1 and 2 spacecraft measurements. That study showed that the shear Alfvén wave in the upper frequency branch is largely confined. The authors concluded that energetic protons could excite the waves, and that these waves would ultimately damp on the electrons due to increasing perpendicular wave number with each successive passing through the equatorial plane. Another study by Mithaiwala *et al.* [16] examined the excitation of this natural resonator by an active neutral gas release. These authors also performed ray tracing studies and showed that the rays did not wander significantly after several reflections in the magnetosphere. They identified that a radial reflection in the group velocity arises due to the off-diagonal component,  $\varepsilon_{xy}$ , of the dielectric tensor. Another investigation has been performed that used ray tracing to determine candidate wave modes for alpha channeling in mirror machines [17]. In a later paper [18], it was determined that the shear waves present in the ion-ion hybrid resonator are ideal for implementing the alpha channeling concept.

The present survey builds on the previous ray tracing studies to assess the properties of possible ion-ion hybrid resonators in other geometries relevant to contemporary laboratory experiments, and with differing plasma parameters. Specifically, ray tracing studies are performed in a geometry relevant to LAPD to assess the importance of radial spreading in determining the low quality-factors (Q) measured [13,14]. Ray tracing studies are also performed in toroidal geometries to understand more clearly whether a resonator could exist within a burning plasma. Because of the large ion temperatures that would exist in such a plasma, finite Larmor radius (FLR) effects for the ions must be included in the dispersion relation. The introduction of finite ion temperature into the problem allows the possibility of

coupling between the shear wave and the ion-Bernstein wave (IBW). Recent minority-heating experiments performed in the Alcator-C Mod tokamak have shown that the compressional wave can experience mode conversion into both shear waves and IBWs at the ion-ion hybrid resonance [19], leading to strong toroidal rotation of the plasma. Numerical simulations have been performed to better understand this observed mode conversion process [20]. While the present study does not address the mode conversion problem, it illustrates the effect of ion temperature on the ray trajectories for burning plasma conditions in ITER.

The manuscript is organized as follows. Section II reviews the ray tracing formulation and details the numerical method used to solve the resulting equations, paralleling the method used by Rauch and Roux [15]. The section also presents expressions for the group velocity that are used in analyzing the results for different plasma devices. Section III examines group velocity contours and ray trajectories relevant to a recent experiment performed in LAPD [13,14], and estimates the quality factors expected for the resonator due to radial spreading of the wave energy. Section IV examines the ray trajectories of waves launched in the Enormous Toroidal Plasma Device (ETPD) [21] and discusses the effects of field-line curvature on the ray. Section V considers ray trajectories of waves in ITER and discusses the implications of finite temperature effects. Section VI summarizes the results.

## II. FORMULATION

### A. Ray Tracing Equations

In formulating the ray tracing equations, the dispersion relation is used to determine the frequency as a function of the wave vector and the plasma parameters (which presumably vary with position but are assumed constant in time in this manuscript). This frequency then becomes the effective Hamiltonian for the ray trajectory with the wave vector playing the role of the canonical momentum [22]. However, the ray tracing equations for the position of the ray,  $\mathbf{r}$ , can alternatively be formulated in terms of the index of refraction [23],  $n$ , and the scaled wave vector,  $\mathbf{v} = \mathbf{k}/k_0$ . In this approach, the ray tracing equations take the form

$$\frac{d\mathbf{r}}{ds} = \frac{1}{n^2} \left( \mathbf{v} - n \frac{\partial n}{\partial \mathbf{v}} \right), \quad (3)$$

$$\frac{d\mathbf{v}}{ds} = \frac{1}{n} \frac{\partial n}{\partial \mathbf{r}}. \quad (4)$$

In Eqs. (3) and (4),  $s$  is a measure of the path length and is related to the time variable through  $s = ct$ .

To apply the previous equations to the situations of interest here, the expression for the index of refraction must be obtained for the shear Alfvén wave. The dispersion relation is extracted from Maxwell's equations with the plasma dielectric included. This leads to the expression,

$$(\epsilon_{\perp} - n^2)(\epsilon_{\perp}\epsilon_{\parallel} - \epsilon_{\perp}n^2\sin^2\psi - \epsilon_{\parallel}\cos^2\psi) - \epsilon_{xy}^2(\epsilon_{\parallel} - n^2\sin^2\psi) = 0, \quad (5)$$

where  $\psi$  is defined as the angle between the confinement magnetic field and the scaled wave vector. It obeys the relation,

$$\mathbf{v} \cdot \mathbf{B}_0 = nB_0 \cos\psi. \quad (6)$$

In Eq. (5), the role of the off-diagonal term of the dielectric tensor is clear; it leads to coupling between the shear and the compressional roots. This is seen by the fact that upon neglecting it, the dispersion relations for the shear wave and the compressional wave are recovered independently for any  $\psi$ . Including this term leads to the expression,

$$n^2 = \frac{b \pm |b| \sqrt{1 - 4ad/b^2}}{2a}, \quad (7)$$

with,

$$a = \epsilon_{\perp} \sin^2\psi + \epsilon_{\parallel} \cos^2\psi, \quad (8)$$

$$b = (\epsilon_{\perp}^2 - \epsilon_{xy}^2) \sin^2\psi + \epsilon_{\perp}\epsilon_{\parallel}(1 + \cos^2\psi), \quad (9)$$

$$d = \epsilon_{\parallel}(\epsilon_{\perp}^2 - \epsilon_{xy}^2). \quad (10)$$

The appropriate sign must be chosen for the shear root. It is not specified here as the choice depends on the value of the wave frequency relative to the cyclotron frequencies of the individual species. From Eq. (7), it is clear that  $n$  only depends on  $\mathbf{v}$  through the angle,  $\psi$ . Differentiating Eq. (6) with respect to  $\mathbf{v}$  results in the expression

$$\frac{\partial\psi}{\partial\mathbf{v}} = \frac{\mathbf{v}B_0 \cos\psi - n\mathbf{B}_0}{n^2B_0 \sin\psi}. \quad (11)$$

In all the following work, the other derivatives are evaluated numerically due to the complexity of the resulting analytic expressions.

In numerically solving the system, it is apparent that there are seven equations that must be satisfied (six from the differential equations, and the seventh, from the dispersion relation requirement that  $|\mathbf{v}| = n$ ) with six unknowns. In this sense, the system is over-determined. Rigorously, the dispersion relation property simply reflects that the Hamiltonian for this system is conserved, and a correct solution of the differential equations must have this property. In practice, however, due to numerical errors, this condition can be violated after a few computational steps are implemented. In order to address this problem, a technique proposed by Yabroff [24] is adopted in which  $\mathbf{v}$  is renormalized after each numerical update so that it maintains the proper length,  $n$ .

In choosing a numerical scheme, due to the computational expense of each function evaluation, a multi-step method is preferred. For the implementation in this study, a fourth order Runge-Kutta scheme is used for the first four time steps, and following that, a fourth order, Adams-Moulton predictor corrector method is used. This enables the time step to be halved or doubled depending on the relative error present in the calculation.

In evaluating the index of refraction, Eq. (7) is sufficient for the cold plasma case as the dielectric components only depend on the frequency, the densities of the relevant species, and the local value of the magnetic field. When ion temperature effects are included,  $\epsilon_{\perp}$  and  $\epsilon_{xy}$  become functions of  $k_{\perp} = k_0 n \sin \psi$  (see Eqs. (17) and (18) in subsection IIB). It naively appears that Eq. (7) can be solved by fixed point iteration. However, this method fails to converge quickly near reflection points. Because of this behavior, Newton's method is used to solve the implicit equation numerically.

## B. Group Velocity

Regardless of how the ray tracing equations are handled, the ray moves along a path determined by the local group velocity. Thus, it is useful to understand the behavior of the group velocity when interpreting the ray tracing results. The parallel and perpendicular group velocities are expressed as

$$v_{g\parallel} = \frac{\partial \omega}{\partial k_{\parallel}}, \quad (12)$$

$$v_{g\perp} = -\frac{\partial k_{\parallel}}{\partial k_{\perp}} v_{g\parallel}. \quad (13)$$

In evaluating these expressions, the cold plasma approximation for the parallel dielectric is used,

$$\varepsilon_{\parallel} \Rightarrow -\frac{\omega_{pe}^2}{\omega^2}. \quad (14)$$

For the perpendicular dielectric and off-diagonal components, both the cold and warm plasma expressions are considered in order to determine the relative effects of finite ion temperature on the rays. The cold plasma expressions are

$$\varepsilon_{\perp} = \left( \frac{c}{v_A} \right)^2 \frac{1 - \frac{\omega^2}{\omega_{ii}^2}}{\left( 1 - \frac{\omega^2}{\Omega_1^2} \right) \left( 1 - \frac{\omega^2}{\Omega_2^2} \right)}, \quad (15)$$

$$\varepsilon_{xy} = \sum_{j=1,2} \frac{\omega_{pj}^2}{\Omega_j^2} \frac{\frac{\omega}{\Omega_j}}{1 - \frac{\omega^2}{\Omega_j^2}}, \quad (16)$$

where  $v_A = B/\sqrt{4\pi\mu_i}$  is the effective Alfvén speed and  $\mu_i$  is the total ion mass density. In these expressions, the frequency is assumed to be on the order of the ion cyclotron frequencies and much less than the electron cyclotron frequency. As a result, the displacement current and the electron contribution have been neglected in  $\varepsilon_{\perp}$ . In  $\varepsilon_{xy}$ , the electron contribution has been partitioned to match each ion contribution to yield the compact expression in Eq. (16). When ion temperature effects are included, the expressions are

$$\varepsilon_{\perp} = \sum_{j=1,2} \sum_{l=1}^{\infty} \frac{\omega_{pj}^2}{\Omega_j^2} \frac{1}{1 - \left( \frac{\omega}{l\Omega_j} \right)^2} \frac{I_l(k_{\perp}^2 \rho_j^2) e^{-k_{\perp}^2 \rho_j^2}}{\frac{1}{2} k_{\perp}^2 \rho_j^2}, \quad (17)$$

$$\varepsilon_{xy} = -\frac{\omega_{pe}^2}{\omega\Omega_e} + \sum_{j=1,2} \sum_{l=1}^{\infty} \frac{\omega_{pj}^2}{\omega\Omega_j} \frac{2}{1 - \left( \frac{\omega}{l\Omega_j} \right)^2} \left( I_l'(k_{\perp}^2 \rho_j^2) - I_l(k_{\perp}^2 \rho_j^2) \right) e^{-k_{\perp}^2 \rho_j^2}, \quad (18)$$

where  $\rho_j$  is the thermal Larmor radius of the j-th ion species, and  $I_l$  is the modified Bessel function of order  $l$ . From these expressions, it is seen that in this approximation,  $\bar{v}_i/v_A \ll 1$ , the dielectric does not depend on  $k_{\parallel}$ , which makes it straightforward to solve the dispersion relation for  $k_{\parallel}$ . The resulting expression is

$$k_{\parallel}^2 = \frac{1}{2} \left[ 2k_0^2 \varepsilon_{\perp} + k_{\perp}^2 \delta_e^2 k_0^2 \varepsilon_{\perp} - k_{\perp}^2 \pm D \right], \quad (19)$$

$$D = \sqrt{k_{\perp}^4 \left( 1 + k_0^2 \delta_e^2 \varepsilon_{\perp} \right)^2 + 4k_0^4 \varepsilon_{xy}^2 \left( 1 + k_{\perp}^2 \delta_e^2 \right)}, \quad (20)$$

with  $\delta_e = c/\omega_{pe}$  the electron skin depth. This expression can be used to evaluate the parallel and perpendicular group velocities leading to

$$v_{g\parallel} = \frac{4k_{\parallel}}{\left[ 2 + k_{\perp}^2 \delta_e^2 \pm k_{\perp}^4 \delta_e^2 \left( 1 + k_0^2 \delta_e^2 \varepsilon_{\perp} \right) / D \right] \frac{\partial}{\partial \omega} \left( k_0^2 \varepsilon_{\perp} \right) \pm 4k_0^2 \varepsilon_{xy} \left( 1 + k_{\perp}^2 \delta_e^2 \right) / D \frac{\partial}{\partial \omega} \left( k_0^2 \varepsilon_{xy} \right)}, \quad (21)$$

$$v_{g\perp} = G + \frac{2k_0^4 \left( 1 + k_{\perp}^2 \delta_e^2 \right) \left( \varepsilon_{\perp} \frac{\partial \varepsilon_{\perp}}{\partial k_{\perp}} - \varepsilon_{xy} \frac{\partial \varepsilon_{xy}}{\partial k_{\perp}} \right) - k_0^2 \frac{\partial \varepsilon_{\perp}}{\partial k_{\perp}} \left[ 2k_{\parallel}^2 + k_{\perp}^2 \left( 1 + k_{\perp}^2 \delta_e^2 \right) \right]}{2k_{\parallel} \left[ 2k_{\parallel}^2 + k_{\perp}^2 - k_0^2 \varepsilon_{\perp} \left( 2 + k_{\perp}^2 \delta_e^2 \right) \right]}, \quad (22)$$

$$G = \frac{k_{\perp} \left[ k_{\parallel}^2 \left( 1 - k_0^2 \delta_e^2 \varepsilon_{\perp} \right) - 2k_{\perp}^2 k_0^2 \delta_e^2 \varepsilon_{\perp} - k_0^2 \varepsilon_{\perp} - k_0^4 \delta_e^2 \left( \varepsilon_{xy}^2 - \varepsilon_{\perp}^2 \right) \right]}{k_{\parallel} \left[ 2k_{\parallel}^2 + k_{\perp}^2 - k_0^2 \varepsilon_{\perp} \left( 2 + k_{\perp}^2 \delta_e^2 \right) \right]}. \quad (23)$$

In the following sections these expressions are evaluated for the relevant machine parameters.

### III. PROPAGATION IN LAPD

To better understand the ray trajectories to be presented, it is useful to first consider the behavior of the group velocity for the relevant plasma conditions. Figure 1 shows color contours of the dependence of the group velocity on perpendicular wave number and scaled frequency, using the cold ion dielectrics in Eqs. (15) and (16). The parameters correspond to those of the recent resonator experiment in LAPD [13, 14]. A hydrogen-helium plasma is considered with concentration ratio  $n_H / n_e = 0.45$  and satisfying charge quasi-neutrality. The electron density is  $n_e = 1.3 \times 10^{12} \text{ cm}^{-3}$ , the magnetic field,  $B = 750 \text{ G}$ , giving an Alfvén speed of  $v_A = 8.85 \times 10^7 \text{ cm/s}$ . Figure 1 displays the components of the group velocity vector as color contours over a relevant range of values of the scaled perpendicular wave number and scaled wave frequency. The top panel, Fig. 1a, illustrates the dependencies of the parallel group velocity, and the bottom panel, Fig. 1b, those of the perpendicular group velocity. On the horizontal axis, the wave frequency is scaled to the cyclotron frequency of helium. In the LAPD resonator experiment this would be equivalent, for a fixed wave frequency, to the axial coordinate along which the strength of the magnetic field varies. On the vertical axis, the perpendicular

wave number is scaled to the electron skin depth and shown over a positive range of values. Note that the color scale for the bottom panel, Fig. 1b, is two orders of magnitude smaller than in Fig. 1a, and also, that it includes positive and negative values since the waves can have a backward character in the perpendicular direction. From these displays, it is clear that for  $k_{\perp} \delta_e > 0.1$  (indicated by the white dashed line), the parallel group velocity is much larger than the perpendicular group velocity resulting in essentially field-aligned propagation. There is a parallel cutoff for the wave at the ion-ion hybrid frequency,  $\omega/\Omega_{He} \approx 2.12$ , represented by the vertical, dashed red line. For higher scaled-frequencies the wave is backward-traveling with the perpendicular phase velocity and the perpendicular group velocity having opposite sign. These are all typical characteristics of the shear wave. As  $k_{\perp}$  decreases towards zero, the perpendicular group velocity switches sign, becoming a forward-propagating wave. In this region the ion-ion hybrid frequency ceases to act as a cutoff, and the wave is no longer field-aligned, having a significant perpendicular component to the group velocity, as is more typical of a compressional mode. However, in LAPD the finite radial dimension of the plasma does not allow these compressional features to play a role, i.e., the window of propagation lies above the white dashed line indicated in Fig.1. Lastly, the peculiar feature at  $\omega/\Omega_{He} = 3.04$  deserves mention. At this frequency the off-diagonal component of the dielectric tensor,  $\varepsilon_{xy}$ , vanishes; since no coupling to the compressional mode exists, the mode remains backward- traveling for all values of  $k_{\perp}$ . For a general two-ion species plasma this behavior occurs at the cross-over frequency,

$$\omega_x^2 = \frac{\omega_{p1}^2 \Omega_2^3 + \omega_{p2}^2 \Omega_1^3}{\omega_{p1}^2 \Omega_2 + \omega_{p2}^2 \Omega_1}. \quad (24)$$

Figure 2 presents horizontal line-cuts of Fig. 1, illustrating the variation of the group velocity components at selected values of the scaled perpendicular wave number. The top panel, Fig. 2a, again corresponds to the parallel group velocity, and the bottom panel, Fig. 2b, to the perpendicular group velocity. The horizontal axis in both plots corresponds to the scaled frequency as in the contour plots of Fig. 1. The four selected curves in each panel use values of  $k_{\perp} \delta_e = 0.086$  (solid), 0.11 (dashed), 0.16 (dashed-dotted), and 0.34 (solid with dotted markers) that correspond to the ray trajectories described in Figs. 6-9, shown later in this Section. The values of  $k_{\perp} \delta_e = 0.086, 0.11, 0.16,$  and  $0.34$  correspond to the solid line and Fig. 6, the dashed line and Fig. 7, the dash-dotted line and Fig. 8, and the dotted line and Fig. 9, respectively. For comparison, the horizontal (white) dashed line in Fig. 1, corresponding to the smallest possible perpendicular wave number in LAPD, has the value of  $k_{\perp} \delta_e = 0.098$ . Thus, the perpendicular wave numbers represented in Figs. 6-9 are representative of those which would be found in the LAPD resonator. From the top panel of Fig. 2, it is apparent that there is very little change in the parallel group

velocity as  $k_{\perp}$  increases over this parameter range. The cutoff is located at roughly the ion-ion hybrid frequency, and the wave continuously slows down as it approaches the hydrogen cyclotron resonance (i.e.,  $\omega = 4\Omega_{He}$ ). The lower panel shows a much more drastic change in the perpendicular group velocity. Due to the inclusion of  $\varepsilon_{xy}$  in the dispersion relation, the perpendicular group velocity is always slightly positive near the ion-ion hybrid frequency, although this effect decreases in importance as  $k_{\perp}$  increases. As  $k_{\perp}$  increases, the line-cuts exhibit the backward-traveling property of the shear Alfvén wave over a larger portion of the frequency range. But at small values of  $k_{\perp}$ , the wave becomes forward-traveling, as the coupling to the compressional mode increases.

Figure 3 illustrates the behavior of the shear-mode dispersion relation when finite ion temperature is included for LAPD conditions. Shown are color contours of the scaled parallel wave number  $k_{\parallel}v_A/\Omega_{He}$  as a function of scaled perpendicular wave number and frequency. The calculation uses Eqs. (17) and (18) in place of Eqs. (15) and (16). The base plasma parameters are the same as in Figs. 1 and 2, but now the ion temperature is set to  $T_i = 1$  eV for both ion species. This results in a ratio of  $\rho_{He}/\delta_e = 0.6$ . The vertical axis is the scaled perpendicular wave number, and the horizontal axis is the scaled frequency. The same scaling factors as in Fig. 1 are used for both quantities. At small values of  $k_{\perp}\delta_e$ , the wave propagates for all frequencies, and exhibits compressional-mode behavior. As  $k_{\perp}\delta_e$  increases, a parallel cutoff appears. Its value starts close to the ion-ion hybrid frequency ( $\omega_{ii}/\Omega_{He} = 2.12$ ), but due to temperature effects it deviates slightly from this value, as indicated by the thick white lines, which correspond to the  $k_{\parallel} = 0$  condition. Two kinetic features appear at the cyclotron harmonics of helium, but they are small effects due to the small temperature considered. An important feature illustrated near the top right quadrant of Fig. 3 is that, for large  $k_{\perp}$ , and frequencies above the third helium harmonic, the contours exhibit a leftward tilt. Because the perpendicular group velocity can be expressed as  $v_{g\perp} = (\partial\omega/\partial k_{\perp})$  with  $k_{\parallel}$  fixed in this partial derivative, the direction of this component of the group velocity can be deduced from the direction that a contour of constant  $k_{\parallel}$  takes in this display format. If the contour moves right (left) for increasing  $k_{\perp}$ , then the wave is forward (backward) traveling.

Figure 4 uses the same display format and color scale as Fig. 1. It illustrates the effects caused by the inclusion of a finite ion temperature to shear-mode propagation in the LAPD plasma, for the plasma parameters of Fig. 3. Again, the (red) dashed line represents the ion-ion hybrid frequency. The first four harmonics of the helium ion are included in the expressions for  $\varepsilon_{\perp}$  and  $\varepsilon_{xy}$  as they fall in the frequency range displayed. The general features are as before with the addition of enhanced perpendicular propagation, indicating ion-Bernstein wave features, especially for frequencies close to the cyclotron harmonics and to the ion-ion hybrid frequency. Also, at larger  $k_{\perp}$  the cutoff-frequency differs from the value of the ion-



ion hybrid frequency. The large perpendicular group velocity near the cutoff can be explained by the departure of the cutoff from the ion-ion hybrid. Figure 5 shows line-cuts of Fig. 4, similar to those in Fig. 2 associated with Fig. 1. The line styles correspond to the same values of  $k_{\perp}\delta_e$  as in Fig. 2. Comparing Fig. 5 to Fig. 2, it can be seen that the perpendicular group velocity is larger near the cutoff when finite ion temperature is included than in the cold ion case; the parallel group velocity is essentially unchanged. Further, a bite-out at  $\omega/\Omega_{He} = 3$  exists due to the cyclotron harmonic response.

With this background, the ray tracing results are now examined. The spatial dependence of the confinement magnetic field used in the resonator experiments in LAPD can be described adequately in cylindrical geometry,  $(\rho, \phi, z)$ , by the expression

$$\mathbf{B}_0 = B_z(z)\hat{\mathbf{z}} - \frac{\rho}{2} \frac{\partial B_z}{\partial z} \hat{\rho}. \quad (25)$$

The axial (z-dependence) of the magnetic well is approximated by the expression

$$B_z(z) = B_{\min} + (B_{\max} - B_{\min}) \tanh^2\left(\frac{z^2}{L^2}\right), \quad (26)$$

where,  $B_{\min} = 750$  G,  $B_{\max} = 1250$  G, and  $L = 182.6$  cm. For the ray trajectories presented in this section, the frequency is  $f = 818$  kHz or  $\omega/\Omega_{He} = 2.84$  at  $B = B_{\min}$ . This frequency value corresponds to that of a candidate resonant eigenmode measured in the experiment. Each ray trajectory is started at the origin of the cylindrical coordinate system. The initial angle,  $\psi$ , between the z-axis and the initial scaled wave vector,  $\mathbf{v}$ , is varied for each ray with the magnitude of  $\mathbf{v}$  determined by the dispersion relation. This initial choice of  $\psi$  sets the value of the perpendicular wavelength, which is mostly invariant along the trajectory; small variations arise due to the radial component of the magnetic field whose magnitude increases with radius.

In determining the resonator quality factor,  $Q$ , due solely to radial spreading of the associated ray, it is useful to start from the definition

$$Q = \omega \frac{U}{P}, \quad (27)$$

where  $U$  is the energy stored and  $P$  is the power lost. The stored energy can be written as  $U = \bar{u}\pi R^2 d$  where  $R$  is the transverse dimension of the device,  $d$  is the spatial extent of the well in the longitudinal direction, and  $\bar{u}$  is an average energy

density stored in the wave across the column of the plasma. The expression for the power lost is  $P = v_{g\perp} 2\pi R du_{r=R}$  with  $u_{r=R}$ , the energy density at the edge of the plasma and  $v_{g\perp}$ , the average perpendicular group velocity over the trajectory of the ray. This can be computed by  $v_{g\perp} = \Delta r / \Delta t$  where  $\Delta r$  is the radial displacement that a ray experiences upon traveling from the center to the reflection point and  $\Delta t$  is the time it takes for the ray to travel this distance. Implicit in this expression is the assumption that all wave energy that reaches the plasma edge escapes. Substituting these expressions into Eq. (27) gives the expression

$$Q = \left[ \frac{\bar{u}}{u_{r=R}} \right] \frac{R}{\Delta r} \omega \Delta t . \quad (28)$$

The factor contained in square brackets is a geometric factor and depends on the radial eigenmode of the system. Taking this factor to be of order unity, an estimate for the quality factor can be extracted from the ray tracing studies. The radius,  $R$ , is taken to be the width of the plasma column which is roughly 20 cm. The remaining parameters can be determined by examining the specific ray in question.

In Figs. 6-9, various ray trajectories in the  $(z, r)$  plane are shown. In each figure, the vertical axis is the  $z$ -axis of the plasma column, and the horizontal axis represents the transverse, radial direction  $r$ . No motion for the rays in the azimuthal direction is considered. The solid curves represent rays calculated using the cold ion dielectric as given in Eqs. (14), (15) and (16). The dashed line uses the warm ion dielectric as given in Eqs. (14), (17), and (18) with an ion temperature  $T_i = 1$  eV for both species. The initial angles are  $\psi_0 = 81.5^\circ, 83.4^\circ, 85.4^\circ$ , and  $87.7^\circ$  for Figs. 6, 7, 8, and 9 respectively, resulting in a higher  $k_\perp$  value for each successive figure ( $k_\perp \delta_e = 0.086, 0.11, 0.16$ , and  $0.34$ , respectively). As mentioned previously, these values correspond respectively to the solid, dashed, dash-dotted, and dotted lines in both Figs. 2 and 5. Note that the length-scale used for the axial direction in Figs. 6-9 is a factor of 100 larger than in the transverse direction because wave propagation is essentially along the magnetic field. Also, Figs. 6-9 display the behavior on small radial scales on the order of centimeters; this is done to aid the reader in understanding the plots. The features of the ray trajectories displayed extrapolate well to larger radii, except that the curvature of the mirror magnetic field causes a slight bowing as the ray propagates between reflection points.

From Fig. 6, it is seen that the perpendicular group velocity reverses direction in both the cold and hot rays as they approach the reflection point. This is in agreement with the contour plots of the group velocity, as shown in Figs. 1 and 4. This feature follows from the fact that, near the midplane ( $z = 0$ ), the wave is a backward wave, hence it focuses radially, while near the reflection layer radial-spreading results because the wave becomes a forward wave. In order for the wave energy to be lost (or not) out of the column, one effect must dominate over the

other. In this case, it is clear that the transverse motion near the reflection point is dominant and causes net wave propagation towards the edge of the plasma. It is also apparent that finite ion temperature leads to enhanced transverse motion near the reflection layer over the cold ion result, as expected from Figs. 1 and 4. In computing the quality factor, Eq. (28) is used here and in all subsequent calculations. It is determined that  $Q = 230$  for the cold ion ray and  $Q = 160$  when ion temperature is included.

It is not necessarily the case that the inclusion of finite ion temperature leads to smaller  $Q$ -values. In the top panel of Fig. 7 and the bottom panel of Fig. 8, it can clearly be seen that little radial wandering occurs due to the balance of the transverse motion near the midplane ( $z=0$ ) and near the reflection layer. This occurs at different initial angles for the cold-ion and warm-ion trajectories due to the increase in the perpendicular group velocity for the warm ions. It is conceivable that, if properly tuned, a ray would perfectly retrace itself and the quality factor due to radial spreading would be infinite, as no radial motion would take place. The quality factors for Fig. 7 are  $Q = 2500$  for the cold-ion ray and  $Q = 430$  for the warm-ion case, while for Fig. 8 these values become  $Q = 130$  and  $Q = 14,000$ , respectively.

For Fig. 9, it is clear that the backward-traveling motion at the midplane ( $z=0$ ) is dominant and leads to the ray quickly traveling to the edge of the plasma. Again, the perpendicular motion of the ray near the reflection layer is more pronounced when ion temperature is included. In this case the quality factors are  $Q = 130$  for the cold ions and  $Q = 360$  for warm ions.

Finally, it must be noted that the assumptions underlying the ray tracing equations are not rigorously satisfied as applied to the LAPD resonator in the axial direction, but in the radial direction they are appropriate. The axial gradient scale length of the confinement magnetic field in the resonator configuration used in LAPD is comparable to the axial wavelength of the candidate eigenmodes. A more accurate eigenmode analysis has been presented elsewhere [14], but it neglected the inclusion of  $\epsilon_{xy}$  and it did not consider the effect of finite ion temperature. The present ray tracing results can, however, be used to obtain an estimate of the effect of ion temperature on radial confinement of the wave energy. These features are useful in understanding later sections of the manuscript, as well as in illustrating properties expected in future discussions of resonator phenomena.

#### IV. PROPAGATION IN ETPD

The background magnetic field in the ETPD is well-described in zeroth-order by a toroidal field which in cylindrical coordinates,  $(\rho, \varphi, z)$ , takes the form,

$$\mathbf{B} = \frac{B_0}{1 + \frac{r}{R} \cos \theta} \hat{\phi}. \quad (29)$$

For the present configuration of ETPD,  $B_0 = 200$  G is the magnetic field strength on axis,  $R = 500$  cm is the major radius,  $r$  is the radial distance from the magnetic axis, and  $\theta$  is the poloidal angle. In the actual operation of the device, a small vertical field (z-component) is applied to create a helical field-line geometry consisting of multiple plasma rings. In this manuscript, the z-component is neglected in order to gain an understanding of the pure effects of field-line curvature on the ray path. The plasma considered consists of two ion species, hydrogen and helium, of equal concentrations with a generic electron density of  $n_e = 1 \times 10^{12} \text{ cm}^{-3}$ , and equal ion temperatures of  $T_i = 10$  eV. Because of the significantly lower magnetic field and much larger ion temperature than is achieved in LAPD, finite ion Larmor radius effects play an important role in the ray trajectories in ETPD.

In the purely toroidal field, two wave propagation invariants exist. The first is the z-component of the wave vector,  $k_z$ . The second invariant,  $m$ , is related to the toroidal component of the scaled wave vector,  $k_\phi = m/\rho$ . For simplicity,  $k_z$  is set to zero, and due to the nature of the magnetic field,  $k_\parallel = k_\phi$  and  $k_\perp = k_\rho$ . Due to the invariant nature of the parallel wave number,  $k_\parallel$  cannot vanish except when it is zero from the outset. This precludes the possibility of a resonator in this environment, but the rays, in principle, can sample the ion-ion hybrid layer due to cross-field propagation. Using the simplified dispersion relation, Eq. (2), which neglects coupling to the compressional wave, and solving for  $k_\rho$  gives

$$k_\rho^2 \delta_e^2 = \frac{m^2}{k_0^2 \rho^2 \epsilon_\perp} - 1 \quad (30)$$

It is clear from this expression that a radial reflection point exists at  $\rho = m/k_0 \sqrt{\epsilon_\perp}$  preventing the ray from traveling to larger radii. As this radial reflection point is approached,  $k_\perp$  becomes small, and the wave starts to exhibit compressional features. This alters the predominantly field-aligned propagation characteristic of the shear mode

Figure 10 illustrates two ray trajectories in ETPD, each corresponding to a frequency of  $\omega/\Omega_{He} = 2.6$  at the starting radius,  $r = 0$  cm. The vertical axis indicates the distance of the ray from the minor axis. The horizontal axis is the time (in  $\mu\text{s}$ ) that is required for the ray to travel from the starting position ( $r = 0$ ) to a given value of  $r$ . The solid curve is a ray calculated with the cold ion dispersion relation, and the dashed curve, a ray that is found from the warm ion expressions. The two dash-dotted lines represent the positions at which the frequency matches the local ion-ion hybrid frequency,  $\omega_{ii}/\Omega_{He} = 2$ , at  $r = -116$  cm, and the third cyclotron harmonic of helium at  $r = 77$  cm, as labeled in the figure. The direction of the

gradient of the magnetic field strength is also shown, increasing for negative values of  $r$ . The ray is launched from an initial position where the  $x$ -axis intersects the minor axis,  $\mathbf{r}_0 = R\hat{\mathbf{x}}$ . The initial wave vector is placed in the plane defined by the vectors  $\hat{\rho}$  and  $\hat{\phi}$  with the angle between the wave vector and the magnetic field set to  $\psi_0 = 88.9^\circ$  and  $k_\rho$  set to a negative value for both the solid line and the dashed line (which, for the dashed line, gives a value of  $k_\perp \delta_e = 0.5$  with  $\rho_{He}/\delta_e = 6.1$  initially). The solid curve illustrates the backward-traveling nature of the shear mode as it initially propagates towards positive values of  $r$ . As it approaches the radial reflection point, at roughly  $t = 120 \mu\text{s}$ , the group velocity switches direction due to transitioning from a backward traveling wave with high  $k_\perp$  to a forward traveling wave with small  $k_\perp$ . This is due to the coupling associated with the  $\varepsilon_{xy}$  term included in the dispersion relation. As  $k_\perp$  continues to decrease, eventually  $k_\rho$  flips sign, and the wave experiences another, more abrupt, radial reflection. The process then occurs in reverse order, but now with a positive  $k_\rho$ . From the ray trajectory, it can be deduced that the toroidal field preferentially increases the value of  $k_\rho$ . This can be understood from Eq. (4). If  $\partial n/\partial \mathbf{r}$  is expanded in terms of the parameters on which it depends,

$$\frac{\partial n}{\partial \mathbf{r}} = \frac{\partial n}{\partial \psi} \frac{\partial \psi}{\partial \mathbf{r}} + \frac{\partial n}{\partial B} \frac{\partial B}{\partial \mathbf{r}}. \quad (31)$$

The first term on the right is a pure curvature effect, and the second term is due to the magnetic field gradient. It is clear from Eq. (30) that the effect of curvature causes  $|k_\rho|$  to decrease from its initial negative value towards zero as the ray travels radially outward (towards positive  $r$ ). Upon reflection,  $k_\rho$  becomes positive, and its value increases as it travels radially inward (towards negative  $r$ ). The result is that the curvature tends to increase  $k_\rho$  as the ray propagates. Similarly,  $\partial n/\partial B < 0$  and  $\partial B/\partial \mathbf{r}$  points radially inward leading to the same effect due to the magnetic gradient. Thus, for the cold ray,  $k_\rho$  is always increasing as it propagates. This curvature effect is not exclusively a two-ion effect, but is present also in a single-ion species plasma when ion temperature effects are negligible. Finally, a comment should be made regarding the two-dimensional representation of the three-dimensional ray trajectory. Because the parallel group velocity is much larger than the perpendicular group velocity over a majority of the ray trajectory, the ray experiences toroidal transits during the course of its motion. For example, at  $t = 120 \mu\text{s}$ , the cold ray experiences roughly three toroidal transits.

The finite ion temperature result for this magnetic configuration contains some features present in the cold result, but to better understand the kinetic effects, the dispersion relation is considered in Fig. 11 and the group velocity, in Fig. 12. Figure 11 illustrates the dispersion relation using the display format of Fig. 3. Again,

the scaled frequency is on the horizontal axis, and the scaled perpendicular wave number is on the vertical axis; the color contours represent the scaled parallel wave number. The  $k_{\parallel} = 0$  boundary is outlined as a thick white line, as before. Figure 12 is the analog of Figs. 1 and 4, using similar axes, with the contours representing the parallel group velocity shown in the top panel and those for the perpendicular group velocity in the bottom panel. The vertical (red) dashed line represents the ion-ion hybrid frequency and would be the cold cutoff in the absence of temperature effects. From Figs. 11 and 12 it is apparent that the inclusion of temperature effects creates a complex structure between each cyclotron harmonic. The wave properties can be separated into three distinct regions based on the relative values of  $k_{\perp}$  and  $\omega$ . At small values of  $k_{\perp}$ , the dispersion relation resembles that of the compressional mode, i.e., it propagates isotropically in the direction of the wave vector and does not resonate strongly with the cyclotron harmonics of helium. At intermediate values of  $k_{\perp}$  (roughly in the range of  $k_{\perp}\delta_e = 0.15 - 0.3$ ) and values of  $\omega$  close to the first and second cutoffs, the wave begins to exhibit more of the shear mode characteristics. This is evident by the regions over which the wave is backward-traveling, and by the small value of the perpendicular group velocity relative to the parallel component. Finally, at larger values of  $k_{\perp}$  and for values of  $\omega$  away from the first and second cutoff, the wave becomes increasingly forward-propagating with increasing perpendicular group velocity. The inclusion of ion temperature introduces new cutoffs (propagation bands) at various frequencies that depend strongly on  $k_{\perp}$ . The nature of the wave at these cutoffs, whether it is forward or backward-traveling, corresponds to the direction of the  $k_{\parallel} = 0$  contour in Fig. 11 as before. These properties are useful in interpreting the ray trajectory represented by the dashed line in Fig. 10. For that ray the initial parameters are chosen such that  $k_{\perp}\delta_e = 0.5$  and  $\omega/\Omega_{He} = 2.6$ , so that the wave starts as forward-traveling. Because  $k_{\rho}$  has a negative value, this leads to inward (negative  $r$ ) propagation. Due to magnetic gradient and curvature effects, the value of  $k_{\rho}$  increases from its negative value towards zero, decreasing the value of  $k_{\perp}\delta_e$ . From Fig. 12(b), it can be seen that there are three distinct regions that the wave must travel through in parameter space as  $k_{\perp}$  approaches zero. In transitioning from one region to the next, the ray changes its direction of radial propagation. It is for this reason that there are five total radial reflections observed in the figure. The radial reflection at  $t = 90 \mu s$  corresponds to the reversal of  $k_{\rho}$  from negative to positive. The two reflections adjacent to this  $k_{\perp} = 0$  point represent that transition from a forward traveling wave to a backward traveling wave at intermediate values of  $k_{\perp}$ . The last two radial reflection points represent the transition from intermediate values of  $k_{\perp}$  to large values where the wave is again forward-traveling. At large values of  $t$ , the wave approaches the third cyclotron harmonic of helium, located at  $r = 77$  cm.

Figure 13 illustrates the trajectories of a bundle of rays launched from the same position and with the same plasma conditions as the ray described in Fig. 10. The rays are all launched at the same frequency ( $\omega/\Omega_{He} = 2.6$ ), but differ with respect to the initial angle,  $\psi$ , between the magnetic field and the wave vector. These angles are both positive and negative  $11.25^\circ, 22.5^\circ, 33.75^\circ, 45^\circ, 56.25^\circ, 67.5^\circ, 78.75^\circ, 84.38^\circ, 84.6^\circ, 85.5^\circ, 86.4^\circ, 87.3^\circ, 88.2^\circ$ , and  $89.1^\circ$ . The survey of opening angles is roughly equivalent to starting each of the rays at a different point along the lines in Fig. 10. The top panel of Fig. 13 corresponds to the cold ion result (the solid curve in Fig. 10), and the bottom panel, to the warm ion result (the dashed curve in Fig. 10). In both panels, time (in  $\mu s$ ) is displayed along the horizontal axis with 150 microseconds corresponding, roughly, to one toroidal transit. The vertical axis on the left side indicates radial displacement from the initial position, with positive values corresponding to the outboard side and negative values to the inboard side of the torus. The vertical axis on the right side shows the corresponding change in the ratio of the frequency to the local value of the cyclotron frequency of helium. In the top panel, it is seen that some of the rays at lower values of positive  $\psi$  are quickly refracted out of the plasma column, in both the positive and negative radial directions. These correspond to low perpendicular wave number and possess compressional wave features. Those with more oblique initial angles are more field-aligned and thus propagate farther before refracting out of the plasma column. Rays whose perpendicular wave vector initially point inward, propagate outward (due to the backward-traveling nature of the wave). As they do so,  $k_\perp$  increases towards positive values until they experience a radial reflection. Thus, the wave energy is predominantly deposited on the inboard side. When ion temperature is included in the analysis, this picture changes. As seen in the lower panel (note that time axis is compressed relative to that of top panel), many rays experience multiple radial reflections as mentioned in the discussion of Fig. 10. Those rays that start with  $k_\perp$  initially pointing outward ultimately arrive at the outboard side of the device, regardless of how many radial reflections occur. Those rays that start with  $k_\perp$  pointing inward are carried to the inboard side of the device due to the large inward radial excursion shown in Fig. 10 near the zero of  $k_\perp$ .

## V. PROPAGATION IN ITER

Next, the dispersion relation and group velocity for ITER burning plasma parameters are considered. Figure 14 is the equivalent of Figs. 4 and 12, but now evaluated for characteristic parameters expected for the ITER device. Accordingly the frequency is scaled to the tritium cyclotron frequency  $\Omega_T$ . A deuterium-tritium plasma is considered with equal concentrations of each species. The total electron density is set to  $n_e = 1.0 \times 10^{14} \text{ cm}^{-3}$ , the magnetic field,  $B = 53 \text{ kG}$ , giving an Alfvén speed of  $v_A = 7.34 \times 10^8 \text{ cm/s}$ . The ion temperature is  $T_i = 10 \text{ keV}$  for both ion species. This results in a ratio of  $\rho_T/\delta_e = 6$ . Only two harmonics are included in the expressions for  $\varepsilon_\perp$  and  $\varepsilon_{xy}$  in this case. For these constant parameters the cold ion-

ion hybrid frequency is  $\omega/\omega_{ii} = \sqrt{1.5} \approx 1.22$ , and is represented by the vertical (red) dashed line in Fig. 14. As before, the top panel, Fig. 14a, corresponds to the parallel group velocity and the bottom panel, Fig. 14b, to the perpendicular group velocity. Note that now the color scales in the top and bottom panels have been increased each by roughly an order of magnitude from those used in Fig. 4 for LAPD. As was seen in the analysis of the ETPD device, three distinct regions of  $k_{\perp}$  and  $\omega$  exist, corresponding to the three different wave properties this mode can have. The  $k_{\parallel} = 0$  contour, indicated by the leading left edge of the contour plot, shows that the wave is backward-traveling near the reflection point, but as this contour approaches its asymptotic limit at large  $k_{\perp}$ , it becomes nearly vertical in the plane and the magnitude of the perpendicular group velocity vanishes. Figure 15 illustrates this property by displaying line-cuts of the group velocity at various values of  $k_{\perp}$ . The horizontal axis corresponds to the scaled frequency, and the vertical axis is the appropriate group velocity. The top panel corresponds to the parallel group velocity, and the bottom panel, the perpendicular group velocity. The values of  $k_{\perp}\delta_e = 0.1, 0.2, 0.3$ , and  $0.4$  correspond to the solid line, the dashed line, the dot-dashed line, and the solid line with dotted markers, respectively. In both panels, the thick tick mark on the horizontal axis indicates the value of the ion-ion hybrid frequency. In the top panel, Fig. 15a, it is clear that the parallel group velocity increases and the wave cutoff moves to lower frequencies with increasing perpendicular wave number. Both effects are attributed to the increasing importance of finite ion Larmor radius effects. The lower panel shows the corresponding perpendicular group velocity. At higher frequencies, the perpendicular group velocity also increases. Near the cutoff, the wave is backward-traveling, but with a smaller perpendicular group velocity as  $k_{\perp}$  increases. The abrupt change in value displayed at the cutoff simply indicates that the perpendicular group velocity does not vanish near the reflection point, a feature previously shown in Fig. 5 for LAPD conditions.

With this understanding, the ray trajectories are now explored in a simplified magnetic geometry representative of a tokamak device. The magnetic field consists of a toroidal field component,  $B_t$ , and a poloidal field,  $B_p$ . In the cylindrical approximation, these fields are

$$B_t = B_0 \left( 1 - \frac{r}{R} \cos \theta \right), \quad (32)$$

$$B_p = \frac{rB_0}{Rq(r)}, \quad (33)$$

where  $B_0 = 53$  kG is the magnetic field at the magnetic axis,  $r$  is the radius from the magnetic axis,  $R = 621$  cm is the major radius,  $\theta$  is the poloidal angle, and  $q(r)$  is the



safety factor. For ease of computation, the safety factor is assumed to have a profile of the form

$$q(r) = 1 + 3 \left( \frac{r}{a} \right)^2, \quad (34)$$

where  $a = 200$  cm is the minor radius of the device. In the numerical ray tracing code used for this case, it is easier to solve the differential equations in Cartesian coordinates, but to write the previous expressions in toroidal coordinates. Because of this, a mapping between the two is helpful, i.e.,  $(\phi, \theta, r) \rightarrow (x, y, z)$  is the toroidal position. These coordinates are connected through the relations

$$\theta = \tan^{-1} \frac{z}{\rho}, \quad (35)$$

$$\phi = \tan^{-1} \frac{y}{x}, \quad (36)$$

$$r = \sqrt{\rho^2 + z^2 + R^2 - 2R\rho}, \quad (37)$$

$$\rho = \sqrt{x^2 + y^2}. \quad (38)$$

The representative burning plasma in ITER is assumed to be an equal mixture of deuterium and tritium with a total electron density of  $n_e = 10^{14} \text{ cm}^{-3}$ . When temperature effects are considered, the ion temperature is taken to be  $T_i = 10$  keV for both ion species. But at this stage, to limit complicating effects, the electron response is taken to be in the inertial regime.

Figure 16 illustrates two ray trajectories in ITER, each at a frequency of  $f = 31$  MHz. This frequency, again, lies within the band in which trapping occurs in a cold plasma. The plane represented is that of a poloidal cross section where the horizontal axis is the radial position as measured from the magnetic axis, and the vertical axis corresponds to the  $z$ -coordinate in Eq. (35). The dashed (black) curves indicate the toroidal magnetic flux surfaces. The solid (blue) curve represents a ray calculated with the cold ion dispersion relation, and the dashed-dotted (red) curve, with ion temperature included. Both rays are launched from an initial position of  $x = 50$  cm,  $y = 0$  cm, and  $z = 20$  cm. The initial wave vector is oriented so that it lies in a plane formed by  $\hat{\mathbf{B}}$  a unit vector pointing in the direction of the total magnetic field and  $\hat{\mathbf{r}}$ , a unit vector pointing normal to the magnetic flux surface. The angle formed between the magnetic field and the initial wave vector is  $\psi_0 = 89.6^\circ$  for the cold ion ray, and  $\psi_0 = 85.7^\circ$  for the warm ion ray. The initial  $k_r$  points towards the

magnetic axis and the initial  $k_{\parallel}$  in the direction of the magnetic field. The direction of the gradient of the toroidal field is illustrated in the upper, right-hand side of the figure. The field gradient causes the wave vector to increase preferentially in the direction opposite to the gradient; the effect exists for both cold and hot ions. The reason for this is presented in the discussion following Eq. (31) in Sec. IV. As in the ETPD case, the quantity,  $k_{\phi} = m/\rho$ , is an invariant of the motion. However, the presence of a poloidal field in a tokamak allows for  $k_{\parallel}$  to vanish at conjugate points, thus creating a resonator configuration.

The cold ray, as illustrated by the solid (blue) curve in Fig. 16, displays the backward-traveling nature of the wave. The ray, initially with a negative  $k_r$ , travels radially outward. As it does so, the effects of both curvature and magnetic gradient as described in Sec. IV, cause the value of  $k_r$  to preferentially increase towards positive values. This causes a radial reflection, which then causes the ray to reverse direction and to move inward across the magnetic flux surfaces. The ray can be seen to wander outward for three bounces before it starts to move inward. The trajectory, and the fact that it retraces itself due to the radial reflection, indicates that the effects of field line curvature and magnetic gradient, in and of themselves, do not destroy the resonator. In fact, due to the induced radial reflections, they serve to focus the energy allowing for constructive reinforcement over the course of multiple transits. It is worth mentioning that at the reflection points along the field line, the conditions for ray tracing break down even though they are well satisfied away from these reflection points. This is in agreement with the study by Rauch and Roux [15]. In their study, they verified that close to the reflection point, the wave equation reduces to Airy's differential equation which confirms that reflection will indeed happen. Their same analysis also applies in the case presented here. Further, this suggests that a WKB analysis would be appropriate for this situation. The distance traveled by a ray between conjugate reflection points is on the order of 10 meters with the parallel wavelength being on the order of 30 cm at  $z = 0$ . The fact that the effective wave potential becomes small near the reflection points indicates that the connection formulas must be used and a quantization condition would result from the WKB analysis. This methodology has been reported by the authors elsewhere [12], but the terms associated with  $\varepsilon_{xy}$  were not included in the analysis.

The dashed-dotted (red) curve in Fig. 16 illustrates a ray trajectory in which ion temperature effects are included. In order to obtain a complete ray trajectory, an additional ray is launched from the same starting position but with the direction of the wave vector reversed, giving a complete passing through the region. Because of the effects of field line curvature and magnetic gradient, the value of  $k_r$  preferentially increases as in the previous cases. From Figs. 13 and 14, it can be seen that the inclusion of hot ion effects causes the reflection point of the wave to decrease below the traditional, cold ion-ion hybrid frequency as  $k_{\perp}$  increases. This causes the reflection point to continuously recede away from the ray as the ray propagates towards the reflection point. Thus, as the ray propagates, it achieves

higher and higher values of  $k_{\perp}$  causing the reflection point to approach the cyclotron frequency of tritium.

To illustrate the expected electron behavior to be encountered, Fig. 17 displays the value of the scaled phase-velocity parameter usually entering in the plasma dispersion function,  $\xi = \omega / \sqrt{2} k_{\parallel} \bar{v}_e$ , where  $\bar{v}_e$  is the electron thermal velocity. The electron temperature is taken to be 10 keV, and  $k_{\parallel}$  is extracted from the hot-ion ray trajectory shown in Fig. 16. The horizontal axis in Fig. 17 corresponds to the distance the ray has traveled (in meters). The values of the solid black curve are given by the left vertical scale, which represents the value of  $\xi$  as the ray evolves. The dashed (blue) curve displays the radial position of the ray as it moves along its trajectory and its value is displayed in the vertical scale on the right of the figure. The dash-dotted line shows where the ion-ion hybrid frequency would be located if warm ion effects were negligible. As can be seen from Fig. 17, the ray travels well past the point where it would traditionally reflect in a cold plasma. The values of  $\xi$  found in Fig. 17 indicate that the electron response is not in the inertial regime. Instead of using Eq. (14), the electrons would better be treated by the adiabatic approximation, i.e., Eq. (14) should be replaced with

$$\varepsilon_{\parallel} \Rightarrow \frac{k_D^2}{k_{\parallel}^2}, \quad (39)$$

where  $k_D = \omega_{pe} / \bar{v}_e$  is the Debye wave number. To gain a qualitative understanding of the change expected, the dispersion relation with adiabatic electrons is considered. It is a relatively straightforward calculation to show that the dispersion relation in this case can be solved for  $k_{\parallel}^2$  resulting in the expression

$$\frac{k_{\parallel}^2}{k_0^2} = \varepsilon_{\perp} + \frac{\pm [b^2 + 4ad]^{1/2} - b}{2a}, \quad (40)$$

where the definitions of  $a$ ,  $b$ , and  $d$  now become

$$a = \frac{k_D^2}{k_0^2} + \frac{k_{\perp}^2}{k_0^2} \varepsilon_{\perp}, \quad (41)$$

$$b = \frac{k_{\perp}^2}{k_0^2} \left[ \varepsilon_{\perp} \left( \frac{k_{\perp}^2}{k_0^2} + \varepsilon_{\perp} \right) + \varepsilon_{xy}^2 + \frac{k_D^2}{k_0^2} \right], \quad (42)$$

$$d = \frac{k_D^2}{k_0^2} \varepsilon_{xy}^2 - \frac{k_{\perp}^2}{k_0^2} \left( \frac{k_{\perp}^2}{k_0^2} \varepsilon_{\perp}^2 + \varepsilon_{\perp} \varepsilon_{xy}^2 \right). \quad (43)$$

Figure 18 shows a contour display of Eq. (40) using Eqs. (17) and (18) for the dielectric tensor components, which include ion temperature effects. The plasma parameters are for ITER values as specified previously. From the display, it is seen that a cutoff now exists for all values of  $k_{\perp}$ . Further, the wave is forward-traveling, as the contours are all moving from left to right in the display plane. Finally, the relevant perpendicular wavelengths are shifted to larger values than would be present in the inertial case. All of this suggests that the ray properties can experience new features that can have important consequences for the resonator behavior, beyond the effects due to hot ions reported in the present manuscript. This indicates that a dedicated study that addresses the consequences of the adiabatic electron response in the ITER environment is warranted.

## VI. CONCLUSION

From the examination of ray tracing trajectories, including finite ion temperature, it is concluded that the low value of the quality factors,  $Q$ , measured in the LAPD resonator experiments [13,14] cannot be attributed purely to radial spreading of the wave energy due to the nonuniform nature of the magnetic well geometry. It is found that the quantitative explanation of the measured  $Q$ -values requires a mechanism which dissipates energy with an effective damping rate at least an order of magnitude larger than the rate at which energy is lost radially by wave convection. It is suggestive that mode conversion processes and/or particle resonances in the nonuniform wave environment must be included to fully describe the behavior of this resonator.

It has been demonstrated that when temperature effects are negligible, and for rays propagating along a curved field line, field-line curvature effects preferentially increase the component of the wave vector in the direction opposite to the curvature of the field line. This, combined with a zero in the perpendicular group velocity, explains the radial focusing effect identified by Mithaiwala et al.[16] in the analysis of a magnetospheric resonator. The radial focusing of the wave enhances energy trapping in resonators that exist along a field line where the curvature is predominantly in one direction. When ion temperature effects are considered, many of the same propagation characteristics are found as in the cold-ion case. However, at sufficiently large temperatures, three regions of parameter space are introduced which determine the qualitative characteristics of the wave. At small values of  $k_{\perp} \delta_e$ , the wave is isotropic and strongly exhibits compressional mode characteristics. At intermediate values, the wave is backward traveling with a cutoff existing close to the ion-ion hybrid frequency, exhibiting shear mode characteristics. At large values, the wave again becomes forward-traveling. A single ray can experience all three regions of parameter space as it propagates through a plasma confined in a toroidal magnetic field, experiencing a perpendicular reflection as it transitions from one region to the next.

When ion temperature effects are negligible in a tokamak device, as may be the case for edge conditions, it is clear from the ray tracing studies that a resonator can exist in such a plasma. The effects of field line curvature cause the ray to be focused radially allowing for many reflections which largely retrace each other. However, when ion temperature effects are included, especially at the core temperatures expected in ITER burning plasmas, it is unclear at the present stage whether the resonator can still exist. The present study identifies that to resolve this issue a future analysis of ray propagation with adiabatic electrons is required.

## ACKNOWLEDGEMENTS

The work at UCLA is sponsored by DOE grant DE-SC0007791. W. A. F. is a Lawrence scholar and his work was performed under the auspices of the U.S. Department of Energy by Lawrence Livermore National Laboratory under Contract DE-AC52-07NA27344.

## REFERENCES

- [1] S. J. Buchsbaum, Phys. Fluids **3**, 418 (1960).
- [2] R. L. Smith and N. Brice, J. Geophys. Res. **69**, 5029, doi:10.1029/JZ069i023p05029 (1964).
- [3] J. Jacquinet, B. D. McVey, and J. E. Scharer, Phys. Rev. Lett. **39**, 88 (1977).
- [4] F. W. Perkins, Nucl. Fusion **17**, 1197 (1977).
- [5] R. Majeski, C. K. Phillips, and J. R. Wilson, Phys. Rev. Lett. **73**, 2204 (1994).
- [6] E. F. Jaeger, L. A. Berry, E. F. D'Azevedo, R. F. Barrett, S. D. Ahern, D. W. Swain, D. B. Batchelor, R. W. Harvey, J. R. Myra, D. A. D'Ippolito, c. K. Phillips, E. Valeo, D. N. Smithe, P. T. Bonoli, J. C. Wright, and M. Choi, Phys. Plasmas **15**, 072513 (2008).
- [7] C. Castaldo and A. Cardinali, Phys. Plasmas **17**, 072513 (2010).
- [8] S. T. Vincena, G. J. Morales, and J. E. Maggs, Phys. Plasmas **17**, 52106 (2010).
- [9] G. G. Borg and R. C. Cross, Plasma Phys. Contr. F. **29**, 681-696 (1987).
- [10] A. V. Guglielmi, A. S. Potapov, and C. T. Russell, Pis'ma Zh. Eksp. Teor. **72**, 432 (2000); JETP Lett. **72**, 298-300 (2000).
- [11] V. E. Moiseenko and E. Tennfors, Plasma Phys. and Control. Fusion **38**, 2133 (1996).

- [12] W. A. Farmer, G. J. Morales, S. T. Vincena, and J. E. Maggs. Proceedings of the 39th European Conference on Plasma Physics and 16th Int. Congress on Plasma Physics, Stockholm, 2012, edited by S. Ratynskaya, L. Blomberg, and A. Fasoli (European Physical Society, Stockholm, 2012), p. P.4064.
- [13] S. T. Vincena, W. A. Farmer, J. E. Maggs, and G. J. Morales, Geophys. Res. Lett. **38**, L11101, doi:10.1029/2011GL047399 (2011).
- [14] S. T. Vincena, W. A. Farmer, J. E. Maggs, and G. J. Morales, Phys. Plasmas, **20**, 012111 (2013).
- [15] J. L. Rauch and A. Roux, J. Geophys. Res. **87**, 8191-8198 (1982).
- [16] M. Mithaiwala, L. Rudakov, and G. Ganguli, J. Geophys. Res. **112**, A09218, doi:10.1029/2007JA012445 (2007).
- [17] A. I. Zhmoginov and N. J. Fisch, Phys. Plasmas **16**, 112511 (2009).
- [18] A. I. Zhmoginov and N. J. Fisch, Phys. Plasmas **19**, 055702 (2012).
- [19] Y. Lin, J. E. Rice, S. J. Wukitch, M. J. Greenwald, A. E. Hubbard, A. Ince-Cushman, L. Lin, E. S. Marmor, M. Porkolab, M. L. Reinke, N. Tsujii, and J. C. Wright, Phys. Plasmas **16**, 056102, (2009).
- [20] N. Tsujii, M. Porkolab, P. T. Bonoli, Y. Lin, J. C. Wright, S. J. Wukitch, E. F. Jaeger, D. L. Green, and R. W. Harvey, Phys. Plasmas **19**, 082508, (2012).
- [21] C. M. Cooper and W. Gekelman, Phys. Rev. Lett. (to be published).
- [22] I. B. Bernstein, Phys. Fluids **18**, 320-324 (1975).
- [23] J. Haselgrove, Report of Physics Society Conference on Physics of the Ionosphere (Cambridge Univ., Cambridge, 1954), pp. 355-364.
- [24] I. Yabroff. J. Res. Natl. Bur. Stand. Sect. D, 65 D(5), 485-505 (1961).

## Figure Captions

Fig. 1. (color online) Contour displays of components of group velocity for upper branch of shear Alfvén wave obtained from cold plasma dispersion relation for LAPD parameters. Ion mixture is 45% H<sup>+</sup>, 55% He<sup>+</sup>, magnetic field strength is 750 G and the electron density is  $1.3 \times 10^{12} \text{ cm}^{-3}$ . Vertical axis is the scaled perpendicular wave number,  $k_{\perp} \delta_e$ , and the horizontal axis, the scaled frequency,  $\omega/\Omega_{He}$ . (a) Parallel group velocity, (b) perpendicular group velocity. Horizontal dashed (white)

line represents lower limit on perpendicular wave numbers allowed in LAPD due to finite radial size. Vertical dashed (red) line represents the ion-ion hybrid frequency. Note that contour scales in panels (a) and (b) differ by two orders of magnitude.

Fig. 2. Line cuts of contour displays in Fig. 1 for selected values of  $k_{\perp} \delta_e$ . (a) Parallel group velocity, (b) perpendicular group velocity. Vertical axis is the corresponding component of the group velocity and horizontal axis, the scaled frequency. The solid, dashed, dash-dotted, and dotted curves correspond to values of  $k_{\perp} \delta_e = 0.086, 0.11, 0.16$ , and  $0.34$ , respectively. The parallel group velocity is largely unchanged over this parameter range while the perpendicular group velocity indicates reflections in the perpendicular direction due to the inclusion of  $\varepsilon_{xy}$  in the dispersion relation. At small values of  $k_{\perp}$ , these reflections are close to  $\omega_x$  given by Eq. (24). As  $k_{\perp}$  increases, the reflections move towards  $\omega_{ii}$  and  $\Omega_H$ . The wave is forward-traveling for frequencies close to  $\omega_{ii}$  indicating a reversal in perpendicular direction as the wave approaches the parallel reflection point.

Fig. 3. (color online) Contour display of dispersion relation for the same LAPD base parameters used in Fig. 1, but now both ion species have a finite temperature of  $T_i = 1$  eV. The vertical axis is the scaled perpendicular wave number, the horizontal axis the scaled frequency, and the contours correspond to the scaled parallel wave number. The  $k_{\parallel} = 0$  contour is given by the white curves. Finite ion-temperature effects appear at the second harmonic of helium where coupling to ion Bernstein waves occurs. A similar feature exists at the third harmonic but is less pronounced. Due to finite Larmor radius effects, the  $k_{\parallel} = 0$  contour no longer converges to  $\omega_{ii}$  asymptotically as  $k_{\perp} \rightarrow \infty$ .

Fig. 4. (color online) Contours of group velocity including finite ion temperature corresponding to conditions used in Fig. 3. To be contrasted to the cold ion case of Fig. 1. Vertical axis is the scaled perpendicular wave number and horizontal axis is the scaled frequency. (a) Parallel group velocity, (b) perpendicular group velocity. Vertical (red) dashed line represents  $\omega_{ii}$ . Finite ion temperature generates features near harmonics of  $\Omega_{He}$  and causes the parallel cutoff to deviate from  $\omega_{ii}$  at large values of  $k_{\perp}$ . A large, perpendicular group velocity is now present near the parallel cutoff. Note that contour scales in panels (a) and (b) differ by two orders of magnitude.

Fig. 5. Line cuts of contour displays in Fig. 4 for selected values of  $k_{\perp} \delta_e$ . (a) Parallel group velocity, (b) perpendicular group velocity. Vertical axis is the corresponding component of the group velocity and horizontal axis, the scaled frequency. Line styles correspond to the same values of  $k_{\perp}$  in Fig. 2. Overall, the qualitative behavior is similar to the cold ion case of Fig. 2 except that a bite-out appears in both components of the group velocity at  $\omega/\Omega_{He} = 3$ , the parallel cutoff moves to

higher frequencies as  $k_{\perp}$  increases, and the perpendicular group velocity is much larger near the parallel cutoff.

Fig. 6. Ray trajectories for LAPD. Vertical axis is the axial displacement of the ray, and the horizontal axis, the radial displacement. The rays are launched from the center of the magnetic well ( $r=0, z=0$ ) with the initial value of  $k_{\perp}$  corresponding to the value associated with the solid curves in Figs. 2 and 5. Note that the axial scale ( $z$ ) is two orders of magnitude larger than transverse scale ( $r$ ) to accommodate the highly field-aligned propagation. The solid curve in Fig. 6 uses cold ions, and the dashed curve includes ion temperature effects. Both rays are predominantly field-aligned exhibiting only slight transverse displacements close to the reflection layer. The transverse propagation near the reflection layer is dominant and causes the rays to wander towards the edge of the plasma.

Fig. 7. Ray trajectories for LAPD with initial value of  $k_{\perp}$  corresponding to the value associated with the dashed curves in Figs. 2 and 5. Top panel (a) uses cold ions, and bottom panel (b) includes finite ion temperature. The top panel shows that the backward-traveling nature of the ray at the center of the well ( $z = 0$ ) is counterbalanced by the forward-traveling nature of the wave near the reflection points resulting in little net transverse motion of the ray even after many transits. This effect is not present in the bottom panel as the inclusion of ion temperature causes increased transverse motion near the reflection point.

Fig. 8. Ray trajectories for LAPD with initial value of  $k_{\perp}$  corresponding to the value associated with the dashed-dotted lines in Figs. 2 and 5. Top panel (a) uses cold ions, and bottom panel (b) includes finite ion temperature. For the top panel, the backward-traveling nature of the ray near the center of the well ( $z = 0$ ) dominates and the ray wanders to the plasma edge. In the bottom panel, the backward-traveling nature of the wave towards the center is balanced by the forward-traveling nature at the reflection point. The resulting ray almost retraces itself.

Fig. 9. Ray trajectories for LAPD with initial value of  $k_{\perp}$  corresponding to the value associated with the solid curve with dotted markers in Figs. 2 and 5. Here the solid curve uses cold ions, and dashed curve includes finite ion temperature. For this wave number the backward-traveling nature of the wave dominates the transverse motion of the ray in both cold and warm ion cases causing the rays to move to the plasma edge.

Fig. 10. Ray trajectories for ETPD. The plasma is comprised of 50%  $H^+$ , 50%  $He^+$  ions with an electron density of  $10^{12} \text{ cm}^{-3}$ . Vertical axis represents radial displacement from the center of the plasma with positive (negative) values representing outboard (inboard) propagation. The horizontal axis is time of propagation with  $150 \mu\text{s}$  roughly equivalent to one toroidal transit. The direction of the magnetic field gradient is shown. This gradient causes the perpendicular wave number to increase in the opposite direction. The two dashed-dotted lines represent the positions



where the wave frequency matches the local values of  $\omega_{ii}$  and the third harmonic of  $\Omega_{He}$ , as indicated. The solid curve illustrates a ray trajectory using cold ions and the dashed curve uses hot ions with  $T_i = 10$  eV. Both rays start with  $k_{\perp}$  initially pointing radially inward.

Fig. 11. (color online) Contour display of dispersion relation for ETPD conditions given in Fig. 10 with magnetic field strength of  $B = 200$  Gauss and hot ions. Vertical axis is the scaled perpendicular wave number, the horizontal axis is the scaled frequency, and the contours are the scaled parallel wave number. The  $k_{\parallel} = 0$  contour is illustrated by the thick (white) lines. The 'S' shape of the contours between helium cyclotron harmonics shows regions with a backward-traveling wave sandwiched between two forward-traveling regions.

Fig. 12. (color online) Contour displays of components of group velocity for conditions given in Fig. 11. Vertical axis is the scaled perpendicular wave number and horizontal axis is the scaled frequency. (a) Parallel group velocity, (b) perpendicular group velocity. The vertical dashed (red) line is the ion-ion hybrid frequency. Regions of forward and backward-traveling waves are seen in the bottom panel.

Fig. 13. (color online) A bundle of rays propagating in ETPD. The vertical axis on the left represents radial displacement from the center of the plasma with positive (negative) values representing outboard (inboard) motion. The vertical axis on the right represents the scaled frequency associated with the radial position of the ray. The horizontal axis is the time of propagation for the ray. (a) Cold ions. Rays with low perpendicular wave number have compressional characteristics and are quickly lost out of the plasma. More oblique rays stay within the plasma column for a greater length of time. Radial reflections cause wave propagation towards the inboard side. (b) Hot ions. Rays with an initial perpendicular wave number pointing towards the inboard side are turned towards the inboard side when  $k_{\perp}$  becomes small enough that compressional features dominate. Rays with perpendicular wave number pointing towards the outboard side propagate towards the third cyclotron harmonic of helium.

Fig. 14. (color online) Contour displays of components of group velocity for ITER conditions. The plasma is comprised of 50% D<sup>+</sup>, 50% T<sup>+</sup> with an electron density of  $10^{14}$  cm<sup>-3</sup>, equal ion temperatures of 10 keV and a toroidal magnetic field strength of 53 kG. Vertical axis is the scaled perpendicular wave number and horizontal axis is the scaled frequency. (a) Parallel group velocity, (b) perpendicular group velocity. Vertical dashed (red) line is ion-ion hybrid frequency. Several of the qualitative features of the group velocity seen in Figs. 4 and 12 are also present. Note that contour scales in panels (a) and (b) differ by two orders of magnitude.

Fig. 15. Line cuts of the contour displays in Fig. 14 for selected values of  $k_{\perp}$ . The values of  $k_{\perp}\delta_e = 0.1, 0.2, 0.3, \text{ and } 0.4$  are represented by the solid curve, dashed curve, dashed-dotted curve, and solid curve with dotted markers, respectively. The small, thick vertical lines at the bottom of each panel represent the ion-ion hybrid frequency. (a) The parallel group velocity. Greater variation between cuts is seen with the rays having larger speed as  $k_{\perp}$  increases. (b) The perpendicular group velocity. The frequency interval over which the wave is backward-traveling shifts to lower frequencies, together with the reflection point, as  $k_{\perp}$  increases.

Fig. 16. (color online) Poloidal projection of ray trajectories in ITER. Vertical axis represents vertical displacement of a ray from the magnetic axis, and the horizontal axis represents the radial displacement from the magnetic axis. The black dashed lines represent the nested flux surfaces. The solid (blue) curve is a ray for which the cold plasma dispersion relation is used, and the dashed-dotted (red) curve uses the hot-ion dispersion relation. Both rays have an initial perpendicular wave number that points towards the magnetic axis. The direction of the gradient of the toroidal field strength is shown; the perpendicular wave number preferentially increases in the opposite direction of this gradient. The cold ray is trapped within the magnetic well. It wanders outward across magnetic flux surfaces before propagating inward due to the perpendicular reflection examined earlier for ETPD. The hot ion result is not confined due to the reflection point moving towards the inboard side of the device as the perpendicular wave number increases.

Fig. 17. (color online) Scaled phase velocity parameter associated with the hot-ion ray in Fig. 16. The horizontal axis is the distance traveled by the ray, which includes toroidal motion. The vertical axis on the left represents the value of the kinetic electron parameter  $\xi = \omega / \sqrt{2} k_{\parallel} \bar{v}_e$  and corresponds to the solid black curve. The electron temperature is 10 keV. The numerical values attained indicate that the electron response is in the adiabatic regime. The vertical axis on the right is the value of the radial displacement of the ray from the magnetic axis and corresponds to the dashed (blue) curve. The dashed-dotted line represents the position of the ion-ion hybrid frequency.

Fig. 18. (color online) Contour display of the dispersion relation of a shear Alfvén wave in the upper branch with adiabatic electron behavior for ITER. The vertical axis is the scaled perpendicular wave number, the horizontal axis is the scaled frequency, and the contours are the scaled parallel wave number. In this regime the wave is always forward-traveling and the values of perpendicular wave number are shifted to much lower values than in the inertial electron case.

## Figures

Figure 1

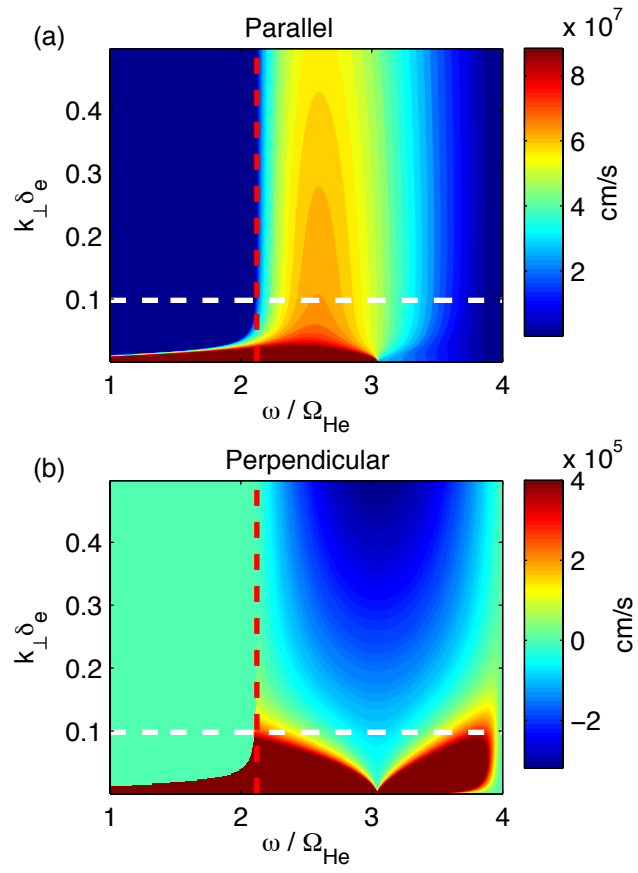


Figure 2

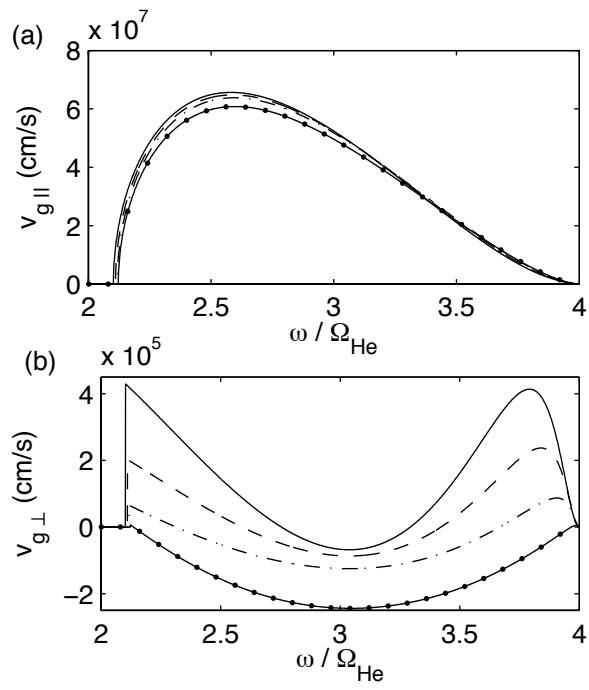


Figure 3

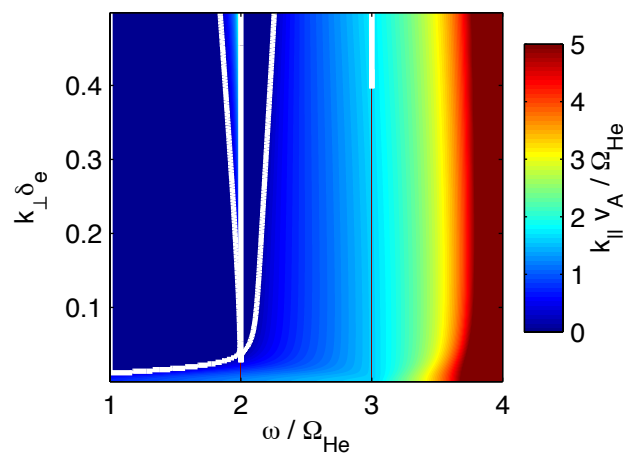


Figure 4

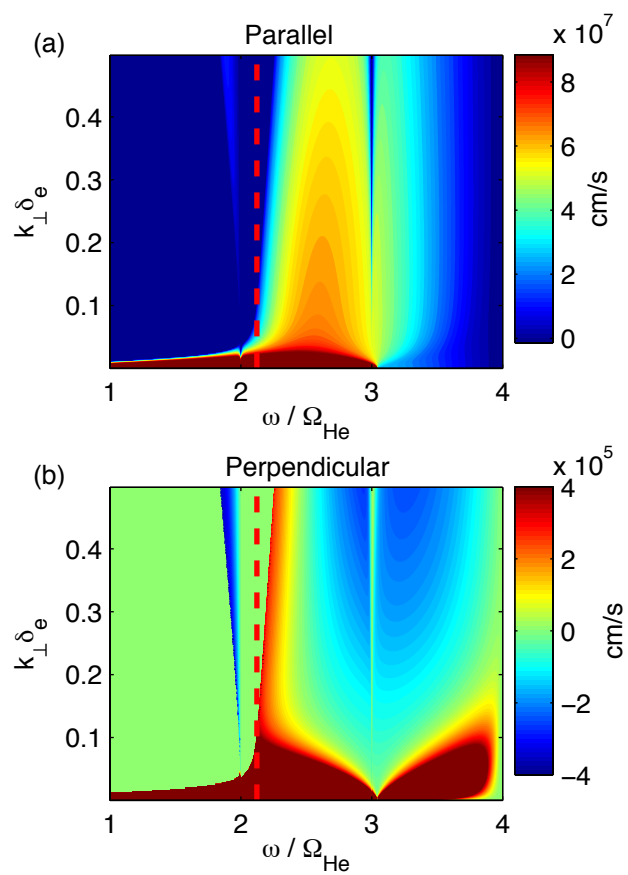


Figure 5

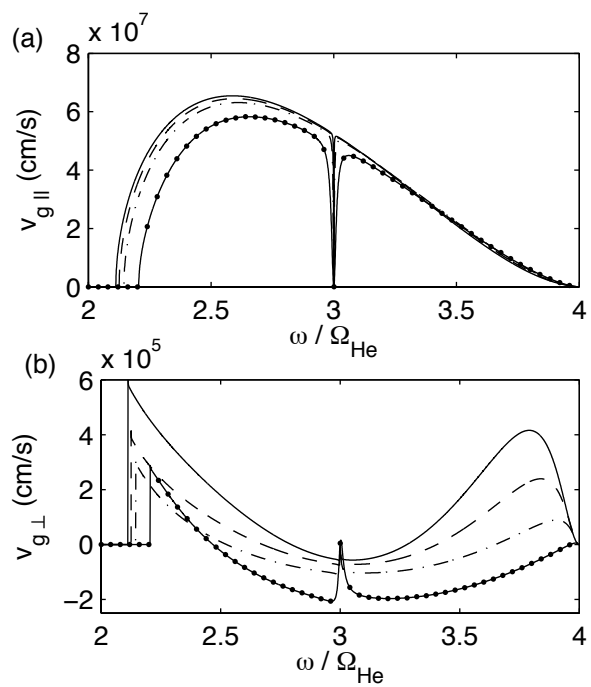


Figure 6

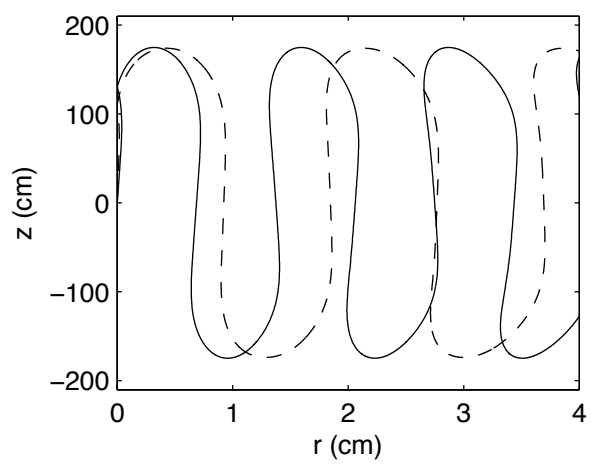


Figure 7

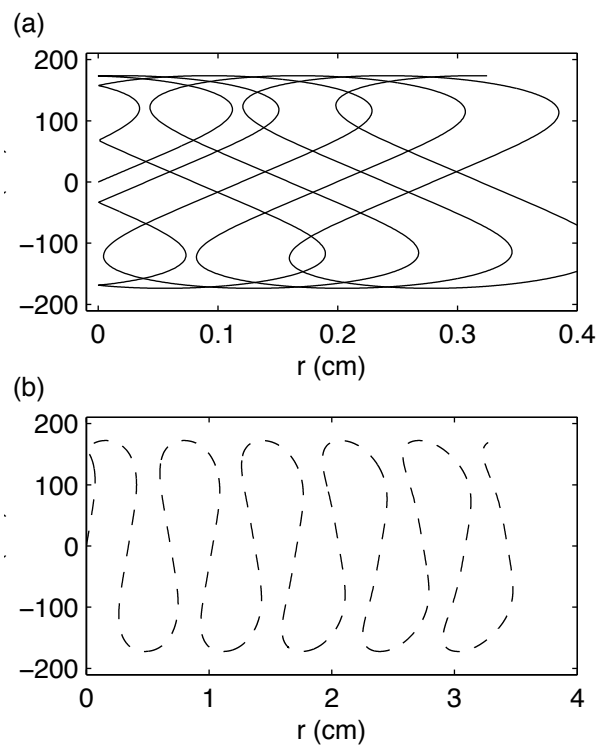


Figure 8

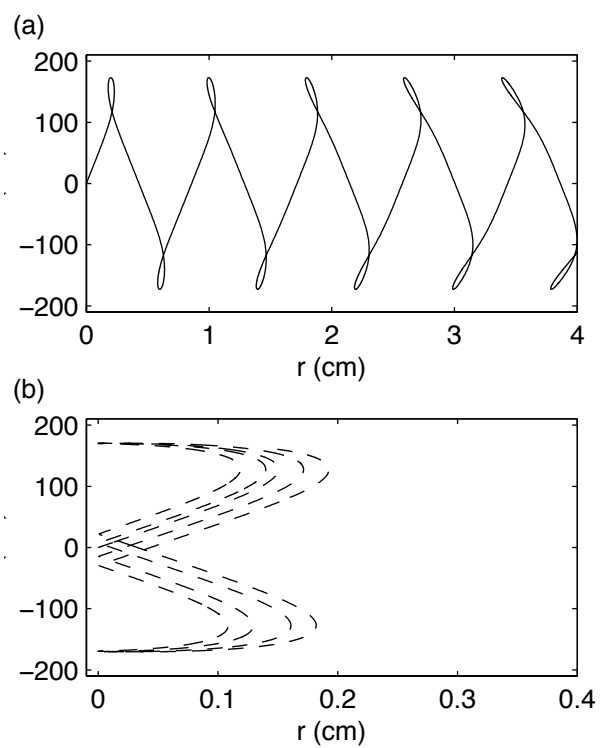


Figure 9

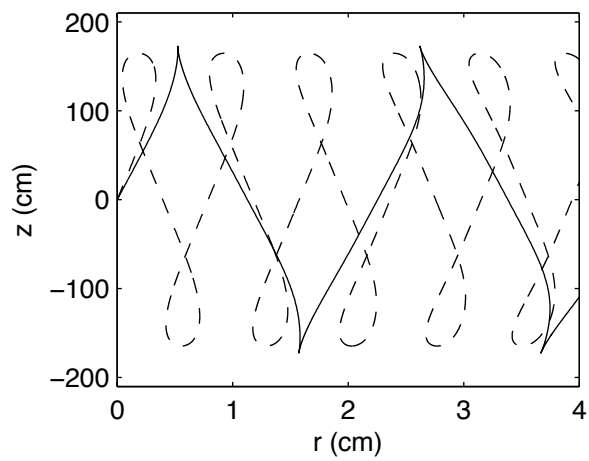


Figure 10

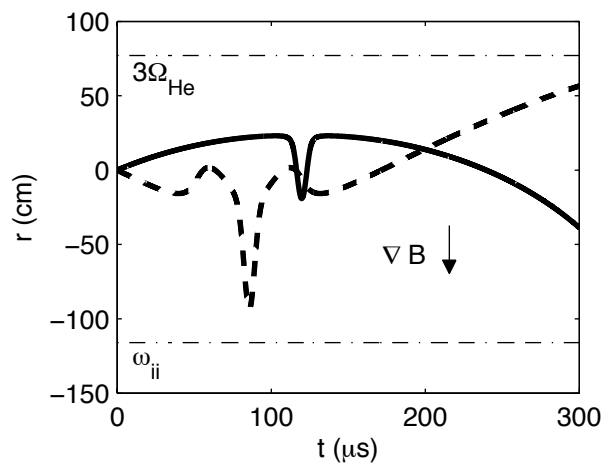


Figure 11

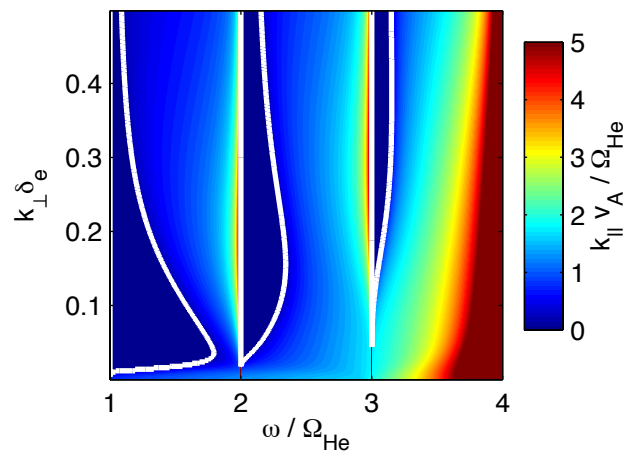


Figure 12

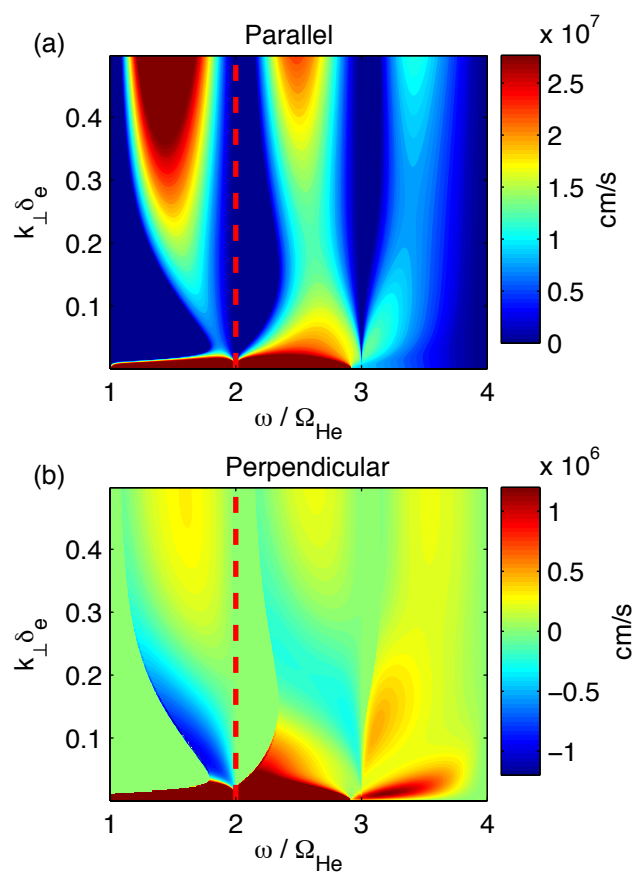


Figure 13



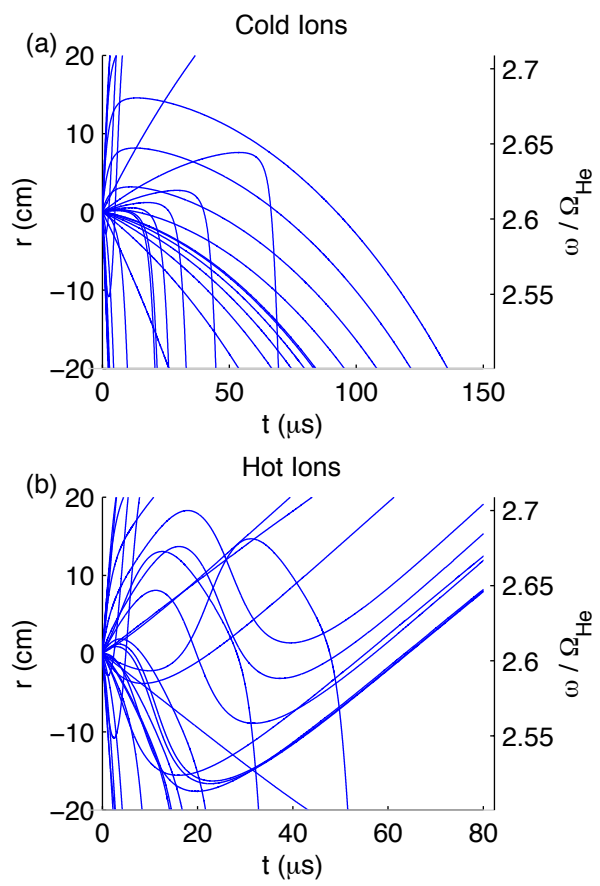


Figure 14

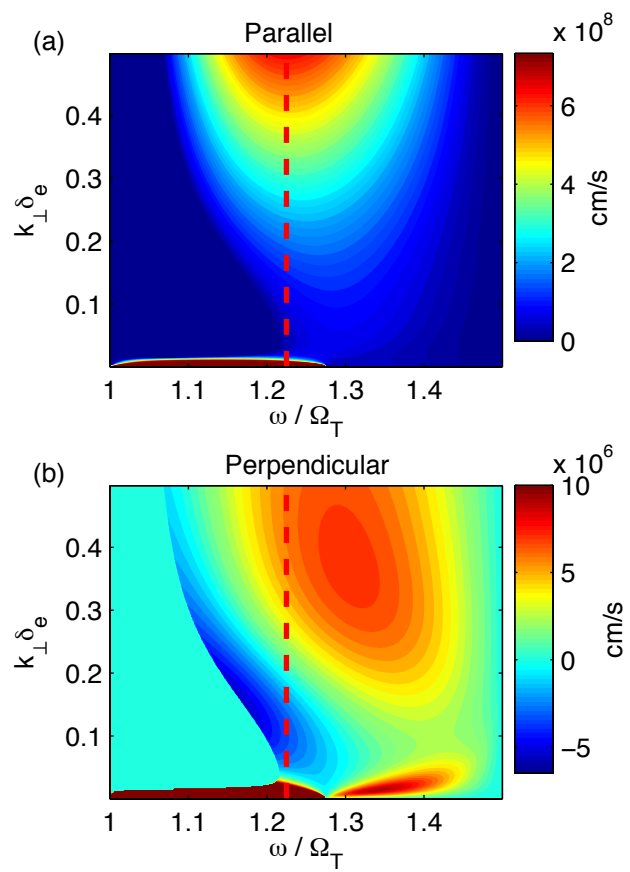


Figure 15

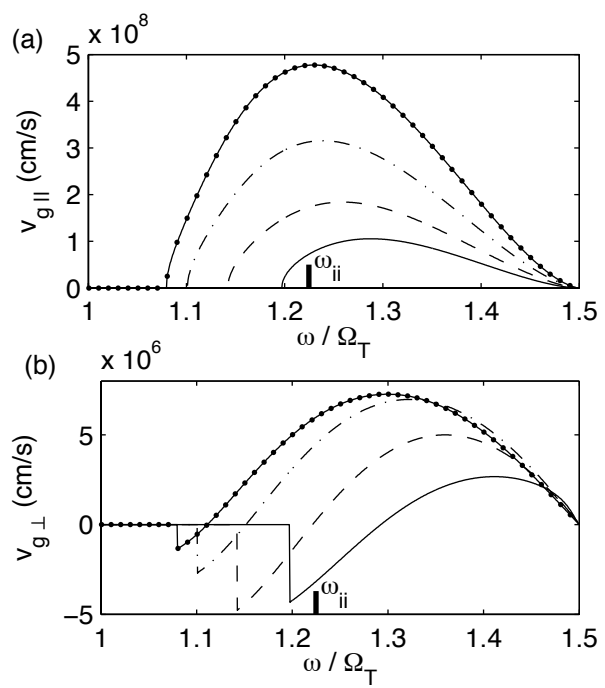


Figure 16

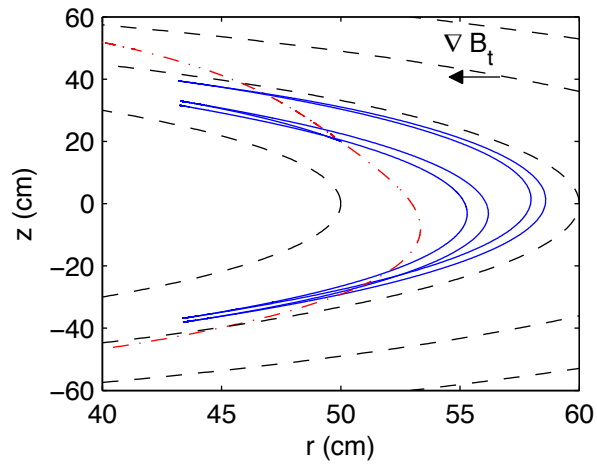


Figure 17

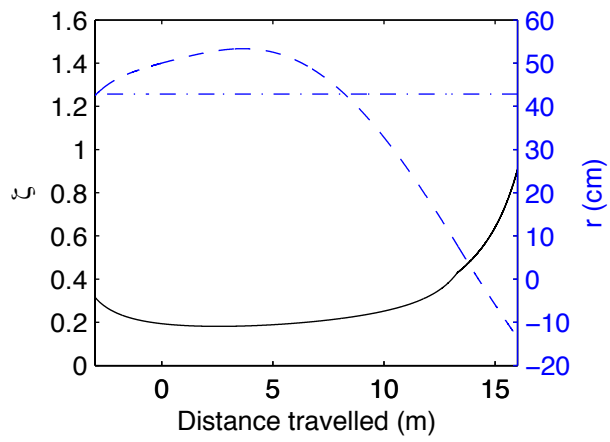


Figure 18

